Optics Letters

High-density integrated delay line using extreme skin-depth subwavelength grating waveguides

Ishtiaque Ahmed,[1,2] Syed Z. Ahmed,[2,3] Nafiz Jaidye,[1,2] Md Borhan Mia,[2,3] Ayrton Bernussi,[2,3] and Sangsik Kim[1,2,3,4,*]

[1]Department of Physics and Astronomy, Texas Tech University, Lubbock, Texas 79409, USA
[2]Nano Tech Center, Texas Tech University, Lubbock, Texas 79409, USA
[3]Department of Electrical and Computer Engineering, Texas Tech University, Lubbock, Texas 79409, USA
[4]School of Electrical Engineering, Korea Advanced Institute of Science and Technology, Daejeon 34141, Republic of Korea
*Corresponding author: sangsik.kim@kaist.kc.ar

Received 23 October 2022; revised 24 January 2023; accepted 16 February 2023; posted 16 February 2023; published 22 March 2023

Optical delay lines control the flow of light in time, introducing phase and group delays for engineering interferences and ultrashort pulses. Photonic integration of such optical delay lines is essential for chip-scale lightwave signal processing and pulse control. However, typical photonic delay lines based on long spiral waveguides require extensively large chip footprints, ranging from mm^2 to cm^2 scales. Here we present a scalable, high-density integrated delay line using a skin-depth engineered subwavelength grating waveguide, i.e., an extreme skin-depth (eskid) waveguide. The eskid waveguide suppresses the crosstalk between closely spaced waveguides, significantly saving the chip footprint area. Our eskid-based photonic delay line is easily scalable by increasing the number of turns and should improve the photonic chip integration density.

https://doi.org/10.1364/OL.479003

An optical delay line is essential in various photonic systems, handling the flow of light in time. With its ability to control phase and group delays, optical delay lines are widely used in interferometers [1], optical fiber communications [2], optical pulse control and buffering [3], quantum computing [4], optical gyroscopes [5], and light detection and ranging (LiDAR) [6]. An integrated photonic delay line is typically implemented using a long waveguide, packed with spiral patterns to save chip footprint. However, to avoid crosstalks between the waveguides, the spacing between the waveguides is set to large (e.g., >10 μm), taking up a considerable area on the mm^2 to cm^2 scale. To reduce the delay line size, approaches such as subwavelength gratings (SWGs) [7,8], linearly chirped contradirectional couplers with Bragg gratings (BG) [9], side coupled integrated spaced sequence of resonators (SCISSORs) [10], multilayer wedge disk silica coupled resonator optical waveguides (CROW) [11], and photonic crystal waveguides (PCW) [12] have been proposed, mostly with a lower group velocity, but the delay line scalability is still limited.

Recently, a waveguide cladded by SWGs was proposed to reduce crosstalk between adjacent waveguides [13,14]. The SWGs form an effectively anisotropic media and reduce the skin depth for lower crosstalk; this scheme is called an extreme skin depth (eskid) waveguide [13]. The SWGs also allow for dielectric perturbations that cancel out the overall coupling coefficient, leading to an infinitely long coupling length [14]. This approach has been shown to miniaturize various integrated photonic devices while enhancing their performance [15–17], but has not yet been applied to the development of an optical delay line.

In this paper, we present a densely integrated photonic delay line using the eskid waveguide scheme and investigate its potential and limitations. A rectangular-spiral delay line is structured with an optimized eskid waveguide, achieving the infinitely long coupling length through anisotropic dielectric perturbations. The delay line is implemented on a silicon-on-insulator (SOI) platform, and its delay time is characterized through monitoring interference patterns and time-domain pulse measurements. The waveguide spacing of our delay line is only approximately 1.0 μm, resulting in a high delay time to footprint ratio. Figure 1(a) shows the schematic layout with an asymmetric Mach–Zehnder interferometer (MZI), including the eskid-based photonic delay line. The input light at the telecommunication wavelength ($\lambda_0 \approx 1550$ nm) is split 50 : 50 and sent to the delay line (red) and the reference arm (blue). Then, they are combined back to the output port, introducing the delay time $\Delta\tau$ between red and blue signals. Y-splitters are used to split and combine the two signals. The delay line is structured via rectangular-shaped spirals, introducing the length difference ΔL than the reference arm. Thus, the delay time introduced to the red signal than blue is $\Delta\tau = \Delta L/v_g$, where v_g is the group velocity of the eskid waveguide.

Figure 1(b) shows the microscopic image of the fabricated delay line region (scalebar: 50 μm). The delay line is formed with rectangular spirals to minimize the bending loss and maximize the straight section lengths. The minimum bending radius is set to 30 μm, and we changed the number of turns N to vary the ΔL. The SWGs at the input and output interfaces of the delay line are also bent so that the strip waveguide mode is adiabatically translated to the eskid mode, avoiding the significant insertion loss caused by the modal mismatch.

Figure 1(c) shows the zoomed-in scanning electron microscope image of the eskid array section in the delay line (scalebar: 2 μm). Our device is fabricated on a 220 nm-thick SOI wafer,

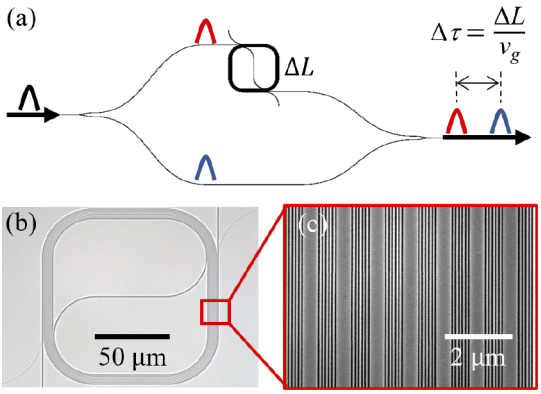

Fig. 1. (a) Schematic of the photonic delay line layout using the eskid waveguide. The input light is split 50 : 50 and sent to the delay line (red) and the reference waveguide (blue) with a length difference ΔL. Then, they are combined, resulting in the delay time $\Delta\tau = \Delta L/v_g$, where v_g is the group velocity of the eskid. (b) Microscopic image of the fabricated delay line and (c) zoomed in scanning electron microscope showing the eskid waveguide.

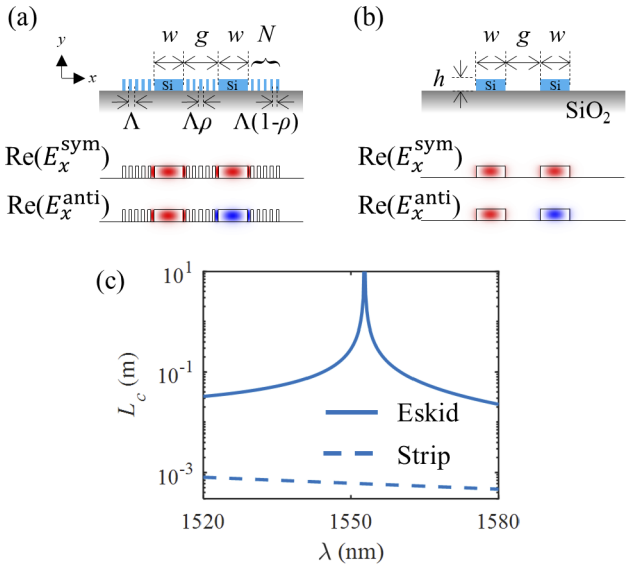

Fig. 2. Schematic cross sections, geometric parameters, and mode profiles of the coupled waveguides: (a) eskid and (b) strip waveguides. (c) Simulated coupling length L_c of the coupled eskid (solid) and strip (dashed) waveguides. The geometric parameters are $h = 220$ nm, $\Lambda = 100$ nm, $\rho = 0.5, N = 5, w = 450$ nm, and $g = 550$ nm.

and the core width is set to 450 nm. Both alternating Si gratings and air gaps of the SWG are set to 50 nm, having the filling fraction $\rho = 0.5$ with a periodicity Λ of 100 nm. This makes the effective indices of SWGs to be anisotropic: from the effective medium theory, $\varepsilon_x = \varepsilon_\perp = \varepsilon_{Si}\varepsilon_{air}/[\rho\varepsilon_{air} + (1-\rho)\varepsilon_{Si}] = 1.847$ and $\varepsilon_y = \varepsilon_z = \varepsilon_\parallel = \rho\varepsilon_{Si} + (1-\rho)\varepsilon_{air} = 6.52$, where $\varepsilon_{Si} = 12.04$ and $\varepsilon_{air} = 1$ (note Fig. 2 for the axis definition). Such anisotropic metamaterial cladding can suppress the skin depth in the evanescent field and introduce anisotropic perturbation, drastically reducing the crosstalk [13,14]. The number of gratings is set to $N = 5$. Note that the gap between the adjacent waveguides is only approximately 550 nm. With a typical strip waveguide scheme, such a short separation distance causes a strong coupling between the waveguides, resulting in significant crosstalk noise. Therefore, a strip-based spiral delay line requires a large separation distance between the waveguides, leading to a substantial device footprint. However, with the eskid scheme, we can minimize the waveguide separation distances while avoiding the crosstalk, miniaturizing the overall footprint area of the delay line.

To quantitatively show the degree of crosstalk, we simulated coupling length L_c of the coupled eskid and strip waveguides. Figures 2(a) and 2(b) show the schematic cross section and mode profiles of the simulated coupled eskid and strip waveguides, respectively. Figure 2(c) shows the simulated L_c spectra for the eskid (solid blue line) and strip (dashed lines) waveguides. Note that, with eskid waveguides, the coupling length is always longer than ≈ 3 cm for the given spectral range, which corresponds to >400 ps delay time (v_g of eskid waveguide is $\approx 7.30 \times 10^7$ m/s). However, with the strip waveguide for the same separation distance, the coupling length is only approximately <0.6 mm, limiting the feasible delay time to <10 ps (v_g of strip waveguide is $\approx 6.51 \times 10^7$ m/s). For this reason, a typical strip spiral delay line requires a larger waveguide spacing, having a high increase rate in footprint per turn (i.e., a longer waveguide length and delay time), while our eskid-based delay line can go up to 400 ps with a dense integration.

The device was fabricated using an electron beam lithography (EBL) on an SOI wafer with 220 nm of Si and 2 μm buried oxide (SiO_2). The die was treated with a solvent rinse followed by O_2 plasma treatment. Hydrogen silsesquioxane (HSQ) was spin-coated on the SOI die and pre-exposure baked on a hotplate. The EBL tool was used to expose the resist at 100 keV energy, with a 500 μm × 500 μm field exposure. Steps were taken to ensure that the EBL selected exposure field for the area of the delay line footprint were all written without any stage movement, while the components were calibrated with drift correction to avoid any stitching or misalignment issue by the movement of the stage. This reduces the stitching error for eskid waveguides and any other components. The resist was developed using 25% tetramethylammonium hydroxide (TMAH). The unexposed top Si device layer was etched using an ICP-RIE etcher with Cl_2 and O_2 gas. An active cooling system was used to ensure a stable stage temperature during the entire etching process. All the devices were fabricated on a single SOI die to minimize process variance. Figures 1(a) and 1(c) show the fabricated device images.

To characterize the delay line performance, four different lengths ($\Delta L = 0.38, 0.48, 0.95$, and 1.07 cm) of asymmetric MZIs were fabricated, whose one arm is connected with the eskid delay line. For the given MZI scheme in Fig. 1(a), the output interference intensity can be represented as [18,19]

$$I = I_1 + I_2 + 2\sqrt{I_1 I_2}\cos(\Delta\varphi), \tag{1}$$

$$\Delta\varphi = \frac{2\pi}{\lambda} n_{\text{eff}}(\lambda)\Delta L, \tag{2}$$

where I_1 and I_2 are the output powers after the reference and delay line arms, respectively, $\Delta\varphi$ is the phase difference between them, and $n_{\text{eff}}(\lambda)$ is the effective index of the eskid waveguide. The wavelength dependency of the effective index can be Taylor expanded around a central wavelength λ_0 and follows [19]

$$n_{\text{eff}}(\lambda) \approx a + b(\lambda - \lambda_0) + c(\lambda - \lambda_0)^2. \tag{3}$$

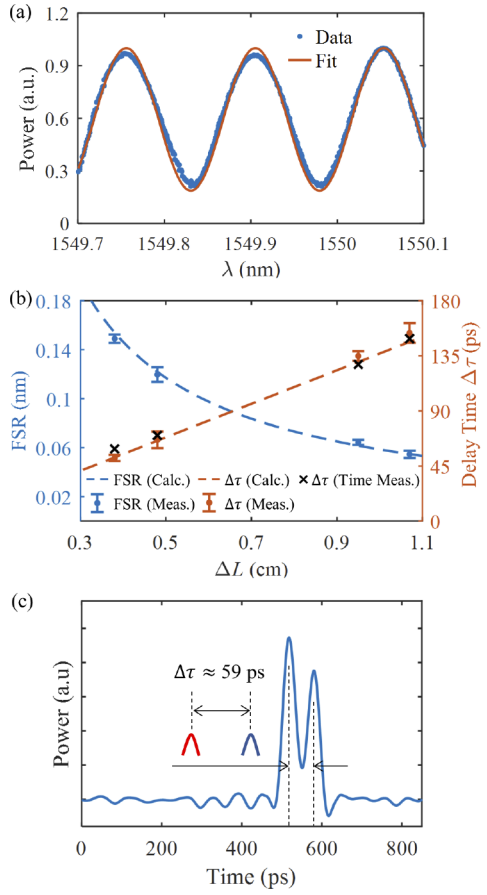

Fig. 3. (a) Measured (blue dots) and fitted (orange line) interference spectrum of the asymmetric MZI with the eskid delay line. (b) Measured (Meas.) FSR (blue dots with error bars) and extracted delay time $\Delta\tau$ (orange dots with error bars) for different lengths ΔL of the delay lines. Dashed lines are numerically calculated FSR (blue) and $\Delta\tau$ (orange). Black crosses represent the characterized delay times by the time-domain measurement. (c) Time-domain measurement of a delayed pulse for $\Delta L = 0.38$ cm MZI. The corresponding delay time is $\Delta\tau \approx 59$ ps.

Then the group index n_g can be represented as

$$n_g(\lambda) \approx a - b\lambda_0 - c\lambda_0(\lambda - \lambda_0). \tag{4}$$

The free spectral range (FSR) of the MZI can be represented as

$$\mathrm{FSR} = \frac{\lambda^2}{n_g \Delta L}, \tag{5}$$

which can be easily measured and characterized.

We measured the transmission spectrum of the asymmetric MZI using a tunable laser source with a 1 pm resolution. A polarization controller was used to set our polarization to be TE mode, and inversely tapered edge couplers were used to interface between fibers and chip. Figure 3(a) shows the measured transmission spectrum (blue dots) of the device when $\Delta L = 0.38$ cm. We fitted the data using Eqs. (1)–(5) to extract the effective index, group index, and FSR of the MZI. Then the delay time was characterized by $\Delta\tau = \Delta L/(c/n_g)$, where c is the speed of light in a vacuum. Figure 3(b) shows the extracted FSR (blue dots) and delay time $\Delta\tau$ (orange dots) for the devices with different lengths $\Delta L = 0.38, 0.48, 0.95$, and 1.07 cm (i.e., $N = 8, 10, 18$, and 20). The measured FSRs for each delay line are $\approx 0.15, 0.12, 0.064$, and 0.055 nm, corresponding to delay times of $\approx 52, 66, 135$, and 154 ps, respectively. The error bars indicate the measurement uncertainty and fitting error from multiple measurements. The dashed lines are the numerically estimated FSR (blue) and delay time (orange) using the simulated group index at 1550 nm, matching well with our experiments.

We also conducted a time-domain characterization using a femtosecond pulse laser with a peak wavelength of 1550 nm and pulse duration of 200 fs. The output signals were detected by a fast photodetector (Thorlabs RXM25AF) and a high sampling oscilloscope (DSO-X91604A). Figure 3(c) shows the measured signals for the asymmetric MZI with a length difference $\Delta L = 0.38$ cm. A clear signal split was detected for a single pulse input with a delay time $\Delta\tau \approx 59$ ps, corresponding to the delay time characterized by the interference signals. We also conducted the same time-domain measurements on the other devices, and they are marked in Fig. 3(b) with black crosses.

For a photonic delay line, a low propagation loss is highly desired as more delay time requires more waveguide length, causing a larger loss. In other words, there is a trade-off between feasible delay time and loss. To characterize the loss of our delay line, we analyzed the interference spectra as in Fig. 3(a). Because the Y-splitter separates optical powers 50 : 50 to each arm, the output power difference between I_1 and I_2 indicates the loss introduced by the delay line, which can be quantified by the modulation depth of the output interference [18]. From Eq. (1), we can express the maximum intensity $I_{\max}$ and minimum intensity $I_{\min}$ as the following:

$$I_{\max} = I_1 + I_2 + 2\sqrt{I_1 I_2}, \tag{6}$$

$$I_{\min} = I_1 + I_2 - 2\sqrt{I_1 I_2}. \tag{7}$$

Since the delay line introduces higher loss, we consider $I_2 < I_1$. By rewriting Eqs. (6) and (7), the loss introduced by the delay line is

$$\begin{aligned} \mathit{Loss}\ (\mathrm{dB}) &= 10\log_{10}\left(\frac{I_1}{I_2}\right) \\ &= 20\log_{10}\left[\frac{(I_{\max} - I_{\min})}{(I_{\max} + I_{\min}) - \sqrt{4 I_{\max} I_{\min}}}\right]. \end{aligned} \tag{8}$$

Using Eq. (8), we characterized the loss of each device, and the blue dots in Fig. 4 show the measured losses from each delay line. Fitting on these loss data (dashed line) indicate the propagation loss is ≈ 3.18 dB/cm, comparable to the previous report [13]. Error bars indicate the facet loss variation of ≈ 0.5 dB. This non-negligible loss limits feasible eskid delay time to <1 ns. The

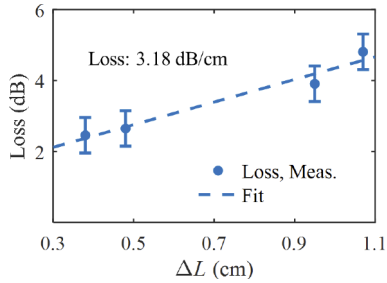

Fig. 4. Loss characterization of the eskid delay line: experimentally measured loss (dots) and fitting curve characterizing the propagation loss (dashed line). Error bars indicate facet loss variations, approximately 0.5 dB.

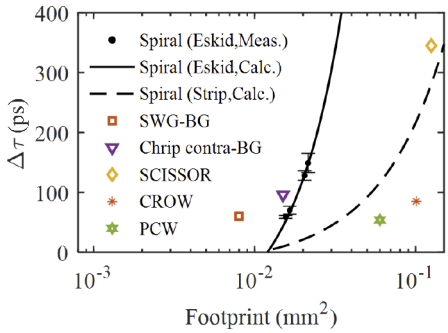

Fig. 5. Delay time $\Delta\tau$ (ps) versus footprint (mm^2) comparison: eskid delay line (solid line, simulation; dots with errorbar, experiments); conventional strip spiral delay line with 10 μm spacing (dashed line); SWG Bragg (orange square) [8]; linearly chirped contradirectional coupler BG (violet triangle) [9]; SCISSOR (yellow diamond) [10]; silica wedge CROW (orange asterisk) [11]; and PCW (green star) [12]. Note the drastic increase in delay time per footprint with the eskid scheme.

sources of the loss might be due to the scattering loss originating from the sidewall roughness, which can be decreased by optimizing post-processing steps such as rapid thermal annealing [20] or depositing a cladding oxide [21].

Since we are employing the eskid waveguide to save the footprint of photonic delay line, we plotted the delay time $\Delta\tau$ (ps) versus chip footprint area (mm^2) in Fig. 5. The estimated (simulated) delay time per footprint of the eskid delay line is plotted with a solid black line, and the black dots with error bars represent our experimental results. For comparison, we also plotted the estimated (simulated) delay time per footprint for a typical spiral delay line (dashed line), assuming a conventional strip waveguide (10 μm separation is assumed). Note the drastic decrease in footprint by using the eskid delay line, whose effect becomes more significant for a longer delay time. Our eskid delay line starts from ≈ 0.013 mm^2 due to the minimum bending radius $R_0 = 30$ μm and the base straight waveguide section length of 50 μm. For comparison, we also mark other delay line schemes, such as chirped SWG Bragg gratings [8], chirped grating contradirectional couplers [9], SCISSORs [10], wedge disk silica CROW [11], and PCW [12]. While some designs exhibit good delay time per footprint, our eskid-based delay line can easily be scaled up by increasing the number of turns. It is also worth mentioning that our eskid-based delay line is arrayed in a very compact area (excluding the empty space in the center); thus, a highly efficient delay time tuning is also expected, for example, using a thermal heater (because the same heat power could affect more area of the thermo-optical index variation).

In summary, we designed and demonstrated a high-density integrated photonic delay line using SWG-based eskid waveguides. The coupled eskid waveguides are optimized to achieve an infinitely long coupling length via anisotropic dielectric perturbations, and such optimized eskid waveguides are packed with a rectangular-spiral structure. Due to its short separation distance between the waveguides, a high delay time to footprint ratio is achieved (≈ 6930 ps/mm^2). Our eskid-based photonic delay line scheme is easily scalable by increasing the number of turns and has a potential for efficient tunability with its dense integration. Our eskid delay line should improve the overall chip integration density, lowering the chip cost and enhancing the chip functionality.

Funding. National Science Foundation (1930784, 2144568); U.S. Department of Energy (DE-NA-0003525); Korea Advanced Institute of Science and Technology (G04220043); National Research Foundation of Korea (RS-2023-00210997).

Acknowledgments. This work was performed, in part, at the Center for Integrated Nanotechnologies, an Office of Science User Facility operated for the U.S. Department of Energy Office of Science by Los Alamos National Laboratory and Sandia National Laboratories. S.K. acknowledges the support by the KSEA young investigator grant.

Disclosures. The authors declare no conflicts of interest.

Data availability. Data underlying the results presented in this paper are not publicly available at this time but may be obtained from the authors upon reasonable request.

REFERENCES

1. D. Melati, A. Waqas, Z. Mushtaq, and A. Melloni, IEEE J. Sel. Top. Quantum Electron. **24**, 4400108 (2018).
2. L. R. Chen, J. Wang, B. Naghdi, and I. Glesk, IEEE J. Sel. Top. Quantum Electron. **25**, 8200111 (2019).
3. M. Moralis-Pegios, G. Mourgias-Alexandris, N. Terzenidis, M. Cherchi, M. Harjanne, T. Aalto, A. Miliou, N. Pleros, and K. Vyrsokinos, IEEE Photonics Technol. Lett. **30**, 31 (2018).
4. K. Vandoorne, P. Mechet, T. Van Vaerenbergh, M. Fiers, G. Morthier, D. Verstraeten, B. Schrauwen, J. Dambre, and P. Bienstman, Nat. Commun. **5**, 3541 (2014).
5. B. Wu, Y. Yu, J. Xiong, and X. Zhang, Sci. Rep. **8**, 8766 (2018).
6. N. Dostart, B. Zhang, A. Khilo, M. Brand, K. Al Qubaisi, D. Onural, D. Feldkhun, K. H. Wagner, and M. A. Popovic, Optica **7**, 726 (2020).
7. Y. Wang, H. Sun, M. Khalil, W. Dong, I. Gasulla, J. Capmany, and L. R. Chen, Opt. Lett. **46**, 1405 (2021).
8. H. Sun, Y. Wang, and L. R. Chen, J. Lightwave Technol. **38**, 5551 (2020).
9. W. Shi, V. Veerasubramanian, D. Patel, and D. V. Plant, Opt. Lett. **39**, 701 (2014).
10. P. A. Morton, J. Cardenas, J. B. Khurgin, and M. Lipson, IEEE Photonics Technol. Lett. **24**, 512 (2012).
11. M.-A. Bianki, C. Lemieux-Leduc, R. Guertin, and Y.-A. Peter, J. Lightwave Technol. **40**, 770 (2022).
12. N. Ishikura, R. Hosoi, R. Hayakawa, T. Tamanuki, M. Shinkawa, and T. Baba, Appl. Phys. Lett. **100**, 221110 (2012).
13. S. Jahani, S. Kim, J. Atkinson, J. C. Wirth, F. Kalhor, A. A. Noman, W. D. Newman, P. Shekhar, K. Han, and V. Van, Nat. Commun. **9**, 1893 (2018).
14. M. B. Mia, S. Z. Ahmed, I. Ahmed, Y. J. Lee, M. Qi, and S. Kim, Optica **7**, 881 (2020).
15. S. Z. Ahmed, I. Ahmed, M. B. Mia, N. Jaidye, and S. Kim, Opt. Lett. **46**, 2164 (2021).
16. M. B. Mia, S. Z. Ahmed, N. Jaidye, I. Ahmed, and S. Kim, Opt. Lett. **46**, 4490 (2021).
17. M. B. Mia, N. Jaidye, I. Ahmed, S. Z. Ahmed, and S. Kim, Opt. Express **31**, 4140 (2023).
18. M. A. Tran, T. Komljenovic, J. C. Hulme, M. L. Davenport, and J. E. Bowers, IEEE Photonics Technol. Lett. **28**, 1517 (2016).
19. S. Dwivedi, A. Ruocco, M. Vanslembrouck, T. Spuesens, P. Bienstman, P. Dumon, T. V. Vaerenbergh, and W. Bogaerts, J. Lightwave Technol. **33**, 4471 (2015).
20. M. G. Wood, L. Chen, J. R. Burr, and R. M. Reano, J. Nanophotonics **8**, 083098 (2014).
21. J. Cardenas, C. B. Poitras, J. T. Robinson, K. Preston, L. Chen, and M. Lipson, Opt. Express **17**, 4752 (2009).